Journal of the Mechanics and Physics of Solids 59 (2011) 64–74

Contents lists available at ScienceDirect

Journal of the Mechanics and Physics of Solids

journal homepage: www.elsevier.com/locate/jmps

Size-dependent heterogeneity benefits the mechanical performance of bone

Haimin Yao [1,2], Ming Dao [1], Davide Carnelli [3], Kuangshin Tai [4], Christine Ortiz *

Department of Materials Science and Engineering, Massachusetts Institute of Technology, 77 Massachusetts Avenue, Cambridge, MA 02139, USA

ARTICLE INFO

Article history:
Received 12 April 2010
Received in revised form
15 August 2010
Accepted 26 September 2010

Keywords:
Biomaterials
Biomechanics
Nanotechnology
Composites
Biomimetics

ABSTRACT

Heterogeneity of biological materials, such as bone, tooth, and mollusc shells, plays a key role in determining their mechanical performance (e.g. the strength, damage tolerance, etc.). Here, we quantify heterogeneities in elasticity and inelasticity of bovine cortical bone between 100 nm and a few microns and identify a characteristic length scale (λ_c) of approximately 200 nm. Below λ_c the mechanical heterogeneity of bone is pronounced and exhibits a strong nonlinear size-dependence, while above λ_c the heterogeneity is much less. Such size-dependent heterogeneity benefits the mechanical performance of bone since it not only promotes the energy dissipation at nanoscale, but also suppresses heterogeneity-induced stress concentration and strain localization at larger length scales. This is one of the possible mechanisms functioning at multiple length scales that make bone a well-designed tough natural material. Utilizing experimentally measured data, systematic computational simulations were carried out, showing that the heterogeneity in inelasticity, rather than elasticity, plays a dominant role in promoting energy dissipation during deformation. Possible parameters that determine the inelasticity heterogeneity (e.g. mean value and standard deviation of heterogeneous yield stress) and therefore affect energy dissipation are investigated under typical deformation modes of bone. The analysis presented suggests that there exists an optimum ratio of macroscopic strength to elastic modulus for improving energy dissipation under tension. All these findings are of great value to the design and synthesis of improved bio-inspired composites.

Published by Elsevier Ltd.

1. Introduction

Heterogeneity refers to the spatial variation of structure and properties in materials. Like most biological materials, bone is a hierarchical structure and exhibits heterogeneity at multiple length scales (Lakes, 1993; Currey, 2005; Fratzl and Weinkamer, 2007). At small length scales (less than a few hundred nanometers) heterogeneity reflects the differences between individual mineralized collagen fibrils and, thus, depends on the internal fibril structure such as molecular orientation, density, size, and shape distribution of hydroxyapatite particles, organic–mineral interactions, etc. (Tai et al., 2007). At larger length scales

* Corresponding author.
E-mail address: cortiz@mit.edu (C. Ortiz).
[1] These authors contributed equally to this work.
[2] Present address: School of Engineering, Sun Yat-sen University, 135 West Xingang Rd., Guangzhou, Guangdong 510275, China.
[3] Present address: LaBS-Laboratory of Biological Structure Mechanics, Department of Structural Engineering, Politecnico di Milano, Piazza Leonardo da Vinci 32, 20133 Milano, Italy.
[4] Present address: Wolfe Greenfield & Sacks, 600 Atlantic Avenue Boston, MA 02210, USA.

0022-5096/$ - see front matter Published by Elsevier Ltd.
doi:10.1016/j.jmps.2010.09.012

(~a few μm), for example within circumferential osteonal bone, heterogeneity exists due to the characteristics of the mineralized fibrils including their orientation, interfaces, and diameter distribution (Wagermaier et al., 2007). At even larger length scale (~10 s of μm), heterogeneity exists because of the periodicity of the osteonal lamellae (Gupta et al., 2006). The detailed structure of the osteon has recently been elucidated via synchrotron X-ray texture measurements and is found to consist of three-dimensional helicoids of mineralized collagen fibrils (Wagermaier et al., 2007). Cellular remodeling processes, which result in composite of "old" and "young" bone, are known to lead to microscopic and nanoscopic heterogeneity (Rho et al., 2002). At the macroscopic level, the mechanical properties of bone are anatomically site-specific (Yeni et al., 2001; Morgan et al., 2003) and vary spatially within a specific anatomical region (Pope and Outwater, 1974). Inspired by these observations, different hypotheses (Phelps et al., 2000; Currey, 2005; Peterlik et al., 2005; Gupta et al., 2006) have been proposed in an attempt to elucidate the possible beneficial or detrimental effects of heterogeneity on the overall mechanical performance of bone. Currently, it is still an open question as to whether heterogeneity is advantageous or disadvantageous to the mechanical functioning of bone.

Within the context of particle or fiber-reinforced engineering composites, it has been well established that a spatially heterogeneous composite microstructure could improve the effective strength and damage tolerance (Brockenbrough et al., 1991; Shen et al., 1994, 1995; Fratzl and Weinkamer, 2007). Recently, it was found through nanoindentation and computational simulations that nanoscale heterogeneity in bone promotes energy dissipation (Tai et al., 2005; Tai et al., 2007). Conversely, mechanical heterogeneity can also introduce or exacerbate stress concentrations and strain localization (Suresh, 2001). The shape, spatial distribution, and volume fraction of the constituent phases can strongly affect the overall mechanical performance (Brockenbrough et al., 1991; Shen et al., 1994, 1995; Munch et al., 2008). Recent studies (Gao et al., 2003; Fratzl and Weinkamer, 2007; Bonderer et al., 2008) indicate that such stress concentration is mitigated when the size of the constituent phases is below a critical dimension (estimated to be approximately 30–200 nm for typical biomaterials). Other characteristic sizes also exist at different length scales and may also play functional roles in bone (Gupta et al., 2006; Kasiri and Taylor, 2008).

Hence, increased heterogeneity can have both positive and negative effects by promoting energy dissipation while simultaneously introducing stress concentrations and strain localization. The mediation of these two conflicting impacts is an essential question for the design of materials with superior mechanical performance. One conceivable way is to have length scale-dependent heterogeneity, whereby at small length scales heterogeneity is pronounced enough to promote energy dissipation, while at larger length scales heterogeneity is much reduced in order to mitigate stress concentrations and strain localization. To investigate this hypothesis in a model biological material, here we examine the size-dependence of heterogeneity in bone. Adult bovine tibial cortical bone (Fig. 1) was employed, of which the osteonal diameter is ~100 μm, the thickness of the individual circumferential lamellae is ~5 μm and the diameter of the individual mineralized collagen fibrils is ~150 nm. Experiments were conducted within individual osteonal circumferential lamellae at the length scales ranging from 100 nm to 2 μm. Moreover, although nanoscale heterogeneity in bone has been shown to promote inelastic energy dissipation during deformation (Tai et al., 2007), the controlling factors and possible routes to maximize this beneficial effect have not been explored completely. In this paper, finite element analysis (FEA) is employed to study the effects of elastic versus inelastic heterogeneity on energy dissipation. Parametric studies are carried out to identify strategies that can maximize energy dissipation. It is expected that the basic concepts discovered in the present study also apply to natural materials other than bone, and could serve as general guidelines for the design of bio-inspired composite materials.

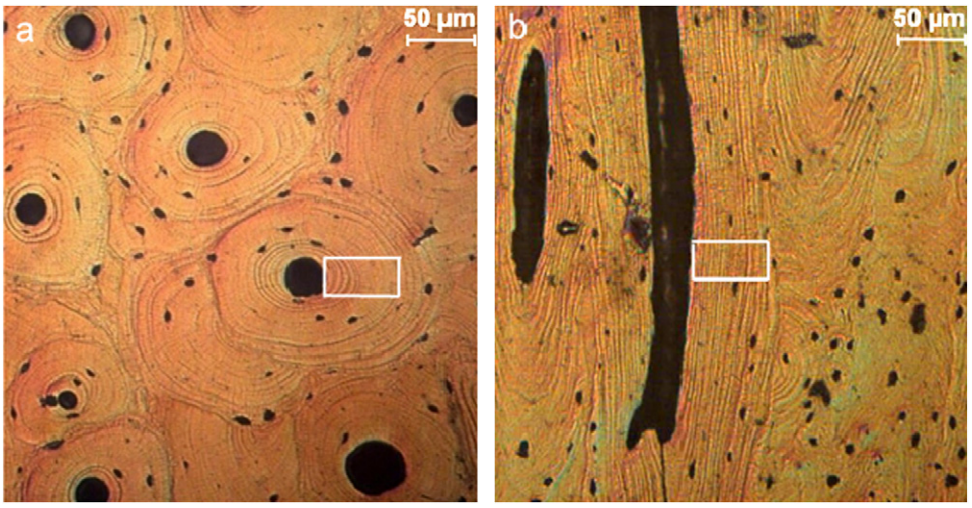

Fig. 1. Optical microscopy images of polished bovine cortical bone: (a) transverse section (cut perpendicularly to the long axis of bone) and (b) longitudinal section (cut parallel to the long axis of bone). Indentation measurements in this study were conducted within the osteonal regions schematically indicated by the white boxes.

2. Size-dependent heterogeneity in bone and its characteristic length scale

To quantify the heterogeneity of bone at multiple length scales, both atomic force microscope(AFM)-based nanoindentation (Tai et al., 2007) and instrumented nanoindentation were conducted in ambient conditions. Adult bovine compact bone from the region between the tibial metaphysis and the diaphysis was cut down to 5 mm cubic specimens using a diamond-impregnated annular wafering saw (Isomet 5000, Buehler, Inc., Lake Bluff, IL, USA) running at 400–600 rpm with constant phosphate buffered saline (PBS, IS=0.15 M, pH 7.4) irrigation. Longitudinal sections (cut parallel to the long bone axis) and transverse sections (cut perpendicular to the long bone axis) were polished using a metallographic polishing wheel (Buehler, at ~100 rpm) and aluminum oxide polishing disk with successively smaller particle grit sizes: 9, 3, 1, 0.3, 0.1, and 0.05 μm (South Bay Technologies Inc.) as well as a microcloth disk (Buehler). Samples were rinsed copiously with deionized (DI) water followed by ultrasonication in DI water between polishing intervals.

To quantify the heterogeneity at the nanoscale, AFM-based nanoindentation experiments were carried out with a constant load of 5 μN and 100 nm inter-indent spacing on 2 μm × 2 μm areas in the ambient environment (21.5 ± 0.7 °C and 50% relative humidity). The maximum indentation depth was evaluated to be <40 nm at a 5 μN maximum load (for ~90% of all of the experimental data) with an average of 30 nm (Tai, 2007; Tai et al., 2007), which corresponds to an average contact diameter of 56 nm. Using the three-dimensional model specified in Tai et al. (2007), the estimated plastic zone size was found to be ~1.6 times the contact diameter. The Oliver–Pharr method (Oliver and Pharr, 1992) was employed to estimate the mechanical properties (indentation modulus and hardness) from the force–depth curves. The spatial distribution of modulus and hardness was mapped using bilinear extrapolation from 20×20 discrete measurements. Eight sets of modulus maps and hardness maps were obtained. Among them, four map sets are from the "axial direction" with indentation loading parallel to the long bone axis, and the other four are from the "transverse direction" with indentation loading perpendicular to the long bone axis. Fig. 2(a) and (b) shows two typical modulus maps corresponding to axial and transverse directions, respectively, with related hardness maps being shown in Fig. 2(c) and (d). The degree of heterogeneity in bone is often described by the coefficient of variation (COV), namely the ratio of the standard deviation to the mean of the property. The COVs for the eight modulus maps range from 0.26 to 0.46 with an average value (± standard deviation) of 0.35 ± 0.07, while the COVs for the related eight hardness maps range from 0.17 to 0.32 with an average value (± standard deviation) of 0.22 ± 0.05. Hence, both modulus and hardness exhibit considerable heterogeneities at the nanoscale, with the maximum and minimum values approximately one order of magnitude apart. In addition to heterogeneity, our results also show anisotropy. The average stiffness in the axial direction is 12.9 ± 4.8 GPa, while that in the transverse direction is only 8.6 ± 3.7 GPa. The ratio between them is around 1.5, in agreement with the orientation-dependent indentation modulus reported in the literature (Ciarelli et al., 2000). It should be pointed out that the minimum inter-indent spacing or spatial resolution (for this experiment, 100 nm) is determined by the size of the plastic zone, which is controlled by the probe sharpness, the material properties of the sample, and the force resolution of the instrument (lower maximum loads result in a reduced size of the plastic zone). To quantify heterogeneity at even lower length scale, experiments using sharper probes are needed.

To quantify the heterogeneity at larger length scales, instrumented nanoindentation experiments were carried out using a Triboindenter (Hysitron, Inc., Minneapolis, MN, USA) with a Berkovich diamond indenter tip (Tai et al., 2005). Experiments were performed under displacement control at four different maximum indenter penetration depths: 50, 100, 200, and 300 nm. For each maximum indentation depth, five sets of indentation tests were performed along the axial and transverse directions, respectively. The corresponding contact diameters at the maximum load obtained using the calibrated tip area function are 372, 692, 1291, and 1898 nm, respectively. Using the FEA indentation model specified in Dao et al. (2001), the estimated plastic zone size was found to be ~1.2 times the contact diameter. A total of 41×3 indentations with a 0.5 μm spacing were performed at 50 nm maximum depth; 31×3 indentations with a 1 μm spacing were performed at 100 nm maximum depth; 21×3 indentations with 2 and 3 μm spacings were performed at 200 and 300 nm maximum depth, respectively.

Based on the nanoindentation measurements above, the modulus COVs at different effective sampling length scales are shown in Fig. 2(e), open diamond symbols. The effective sampling length scale is given as the contact diameter at the maximum load multiplied by a correction factor. Here the correction factor is taken as the ratio of the plastic zone size versus the contact diameter. The variation of COV with the effective sampling length scale observed in this dataset can be well described by an exponential decay function:

$$\mathrm{COV} = \alpha \exp(-l/\lambda) + C \tag{1}$$

where l is the relevant effective sampling length scale, λ is the characteristic length scale beyond which the level of heterogeneity as quantified by COV is quickly reduced to a relatively small base value C, and α is a constant. The best fitting function, as shown by the dash-dotted line (Fig. 2e), has an R^2 of 0.997 and the related characteristic length scale λ_{ind} is estimated to be 228 nm.

The mechanical property measured via indentation can be approximately interpreted as the volumetric mean of the property within the vicinity of the indented region. A simpler alternative methodology, rather than the above experimental approach, can be used to derive the size-dependent heterogeneity. In the following, this methodology is illustrated using the nanoscale heterogeneity maps of Fig. 3(a)–(d).

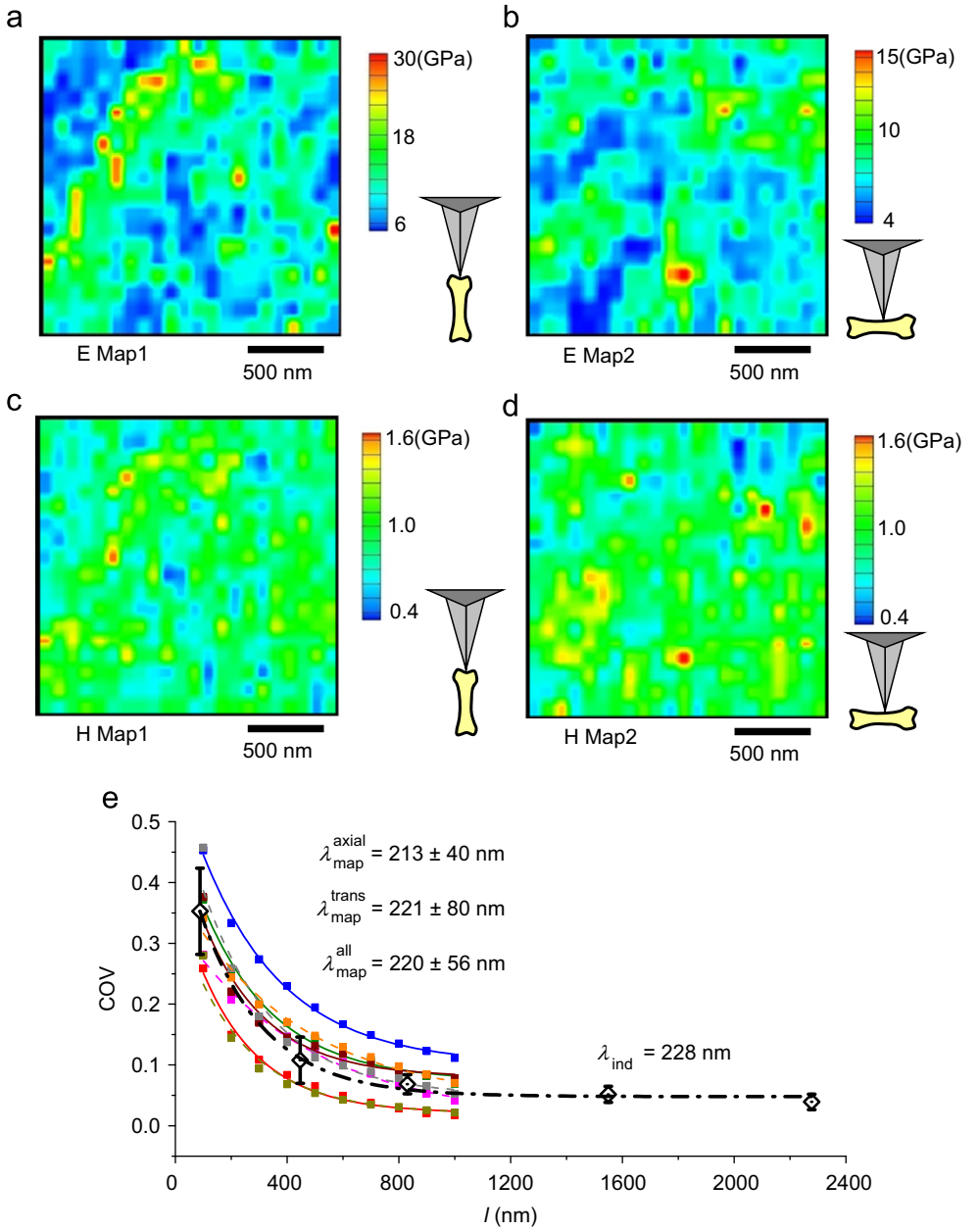

Fig. 2. Typical modulus maps ((a) and (b)) and hardness maps ((c) and (d)) reduced from AFM-based nanoindentation conducted on 2 μm × 2 μm areas. (a) and (c) correspond to the cases with indentation direction parallel to the long bone axis (axial loading), while (b) and (d) correspond to the cases with indentation direction perpendicular to the long bone axis (transverse loading). Bilinear extrapolation was used to obtain a continuous spatial distribution. Open diamond symbols with error bars in (e) show the size-dependent COV of modulus evaluated by nanoindentation tests at different effective sampling sizes; the 1st diamond symbol is taken from AFM-based nanoindentations while the rest are from nanoindentations using a Berkovich tip. Solid square symbols with fitting lines in (e) show size-dependent COVs calculated from the AFM-based nanoindentation maps, where solid lines are from axial loading cases and dashed lines are from transverse loading cases; here the effective sampling size l is taken to be the length of a side of the sampling square.

Suppose we need to determine the heterogeneity of bone at a sampling length scale, l=200 nm, a volumetric (areal for current 2D case) average of a 200 nm × 200 nm region within a map shown in Fig. 2 can be taken as a virtual "measurement" of its local effective property. After randomly taking sufficient number (n) of such virtual "measurements", the COV at the length scale of 200 nm can be evaluated. If we consider 100 nm, the inter-indent spacing of AFM-based nanoindentations, as the smallest representative/effective sampling size in Fig. 2(a)–(d), this methodology can be extended to any sampling length scale $l > 100$ nm. Here we only considered cases with $l = m \times 100$ nm, where m is the integer greater than 1. Without affecting the COV evaluation, we forced the four sides of a sampling square to align with the sides of the 100 nm × 100 nm grids, so that an exhaustive set of virtual measurements can be easily taken. Considering the limited map

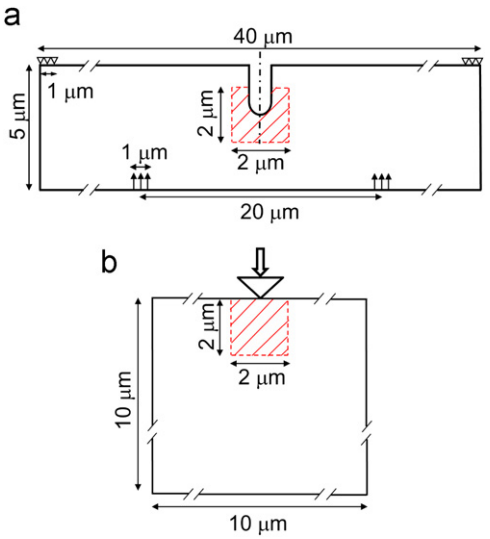

Fig. 3. Schematics of the finite element models used for simulations: (a) 4-point bend model and (b) 2D indentation model. The material properties within the shaded areas were assigned the experimentally extracted (heterogeneous) values and those outside the shaded areas were assumed homogeneous and elastic, and assigned as the effective average elastic modulus.

size ($2\ \mu m \times 2\ \mu m$) of the data shown in Fig. 2(a)–(d), m cannot be too large; otherwise, a sufficient number of virtual measurements (n) cannot be ensured.

Taking m from 1 to 10, the solid colored symbols in Fig. 2(e) show the variation of COVs of modulus (elasticity) as a function of the effective sampling length scale, l, spanning from 100 nm (n=400) to 1 μm (n=100). Eight maps including Fig. 2(a) and (b) were considered. Here, the COVs derived from all eight maps decrease monotonically as the length scale increases. The size-dependence of COVs using this methodology fits well with Eq. (1) with R^2 ranging from 0.981 to 0.996, as shown by the solid and dashed lines for axial and transverse cases, respectively. For the four axial modulus maps, the average characteristic length scale is evaluated to be $\lambda_{map}^{axial} = 213 \pm 40$ nm; for the four transverse modulus maps, $\lambda_{map}^{trans} = 221 \pm 80$ nm; and for all eight maps, $\lambda_{map}^{all} = 220 \pm 56$ nm. This compares reasonably well with λ_{ind}=228 nm evaluated using the experimental nanoindentation data.

Here, we mainly discussed the size-dependence of the heterogeneity in modulus (elasticity). A similar trend is observed from the heterogeneity of hardness (inelasticity). It is clear that bone exhibits size-dependent heterogeneity in both elasticity and inelasticity. There exists a characteristic length scale $\lambda_c \approx 200$ nm below which the heterogeneity is much more pronounced with strong size-dependence while above this characteristic size the effective heterogeneity is much lower. Noting that the type-I collagen fibrils of the adult bovine tibial cortical bone is ~150 nm in diameter (Tai et al., 2005), and the extracted characteristic length λ_c (Fig. 2e) is about 1–2 times the size of collagen fibrils.

3. Effect of elastic versus inelastic heterogeneity on energy dissipation

Bone, as a material with nanoscale heterogeneity, has been shown to promote energy dissipation in comparison to a homogeneous material with equivalent effective properties (Tai et al., 2007). It was shown above that heterogeneity exists in both elasticity and inelasticity. A fundamentally important question thus arises. What are the relative contributions of elastic heterogeneity versus inelastic heterogeneity to the promotion of energy dissipation during deformation? The experimentally measured modulus and hardness maps allow us to investigate this question via parametric finite element computations. Considering the typical deformation modes of bone, a 2D plane-strain four-point bend model and a 2D indentation model were created, as shown in Fig. 3. The material properties within the shaded $2\ \mu m \times 2\ \mu m$ areas were assumed elastic–perfectly-plastic and assigned as the heterogeneous properties obtained from AFM-based nanoindentation. It has been shown that for a strain hardening/softening law, the elastic–perfectly-plastic average yield stress prediction is more suitable given that the parameters are manageable and that the nanoindentation behavior can still be captured (Tai, 2007). Materials outside the shaded area were assumed homogeneous and elastic and assigned as the average elastic properties of the shaded heterogeneous region. For the shaded heterogeneous region, the Young's modulus E is evaluated directly from the load–depth curves with a reasonable estimation of the Poisson's ratio. In order to evaluate the yield stress σ_y, Tai et al. (2007) took a constant elastic-limit-strain assumption and thus correlated E and σ_y through $\sigma_y = \varepsilon_y E$, where ε_y is determined from the indentation force–depth curves. In the present study, a different approach was taken so that σ_y would not depend on E. Assuming that the yield stress is correlated with the hardness through $\sigma_y = cH$, where c is a constant ranging from 0.3 to 0.6 (Pharr and Bolshakov, 2002; Feng et al., 2007) and commonly taken as 1/3 (Gouldstone et al., 2007), σ_y maps can be readily evaluated from the hardness H maps. After assigning a set of E and σ_y

maps into the heterogeneous region of the FEA models, the energy dissipation of bone during deformation can be quantitatively assessed now. Here energy dissipation is defined as the plastic dissipation energy ($\int_V \sigma_y d\varepsilon_p$). Assuming four sides of a heterogeneous microstructure has the same chance to undergo external load; three additional cases can be derived from each simulation case proposed above just by 90°, 180°, and 270° rotations of the examined heterogeneity map set. Here two original axial map sets (out of four) and two original transverse map sets (out of four) were selected for detailed parametric study, thus a total of $4\times(2+2)=16$ cases were studied.

In order to decouple the contributions of heterogeneities in elasticity and inelasticity to energy dissipation, for each simulation case three virtual control cases were considered. The first control case incorporates the heterogeneity of σ_y but assumes homogeneous E. Conversely, in the second control case σ_y is assumed homogeneous, while the heterogeneity of E is incorporated. In the third control case, both E and σ_y were assumed homogeneous. In each control case, the homogeneous properties were taken as the volumetric average of the heterogeneous counterpart. Given load, the energy dissipation D for each control case and the original case was computed. Comparative studies of D between four cases (one original and three controls) can help to identify the individual contributions of elastic heterogeneity and inelastic heterogeneity to energy dissipation.

Fig. 4 shows the relative change of energy dissipation induced by the heterogeneities in E and σ_y. While Fig. 4(a) and (c) is based on the 4-point bend model, Fig. 4(b) and (d) is obtained from the 2D indentation model. Here each data point represents the mean value of the 16 cases. In order to determine whether the heterogeneities in E and σ_y can cause statistically significant variations in energy dissipation, one-sample t-Test was carried out by using Origin (OriginLab Corporation, Northampton, MA, USA). This test assessed whether the mean relative change in energy dissipation is greater than 0 (the *alternative hypothesis* in t-Test) or, in other words, heterogeneity leads to enhanced energy dissipation. The error bars in Fig. 4 denote 95% confidence intervals with the p-values shown aside. Therefore, at the 0.05 significance level, low values of p (<0.05) suggest statistically significant enhancement in energy dissipation, while high values of p (≥ 0.05) imply no significant improvement.

It can be seen from Fig. 4(a) that in the 4-point bend model elastic heterogeneity causes an average of ~5% decrease, rather than an increase, in energy dissipation, no matter the inelastic properties are spatially heterogeneous or homogeneous. The p-values are around 0.8 or even higher, showing no statistically significant increase in energy dissipation for the cases studied in Fig. 4(a). It is particularly interesting to note that there are five cases with p-values

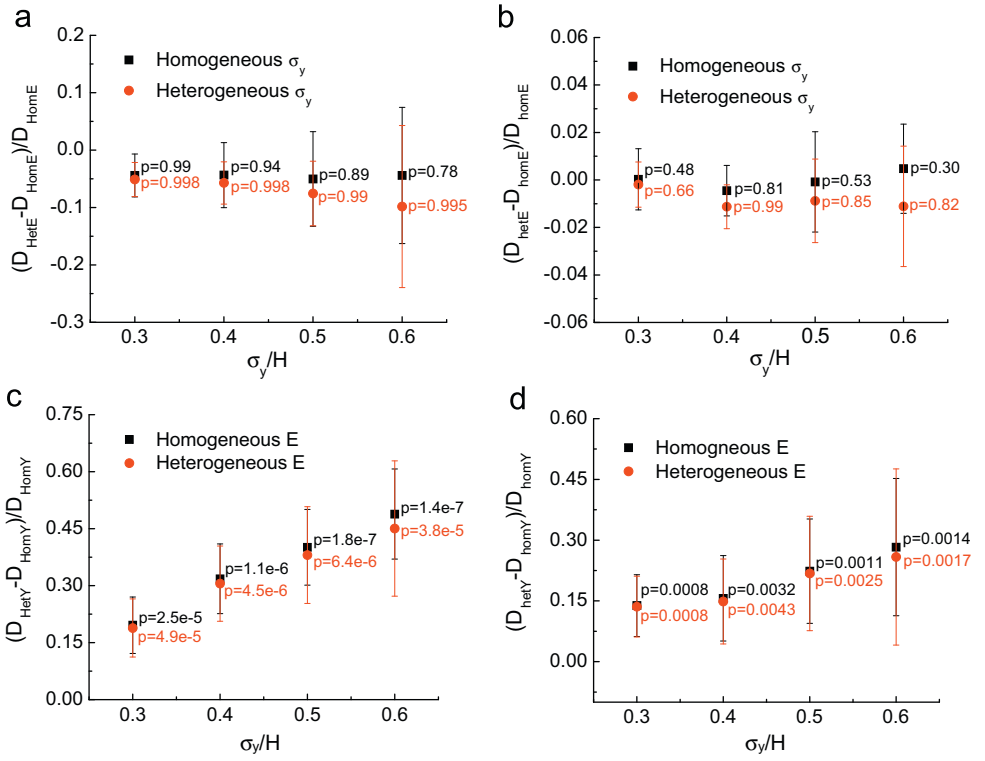

Fig. 4. Relative changes of inelastic energy dissipation due to heterogeneity in elastic modulus ((a) and (b)) and inelastic yield strength ((c) and (d)) for different values of σ_y/H. (a) and (c) are the results from the 4-point bend model, while (b) and (d) are from the 2D indentation model. Here each data point stands for the mean value of the 16 subcases. Error bars denote the 95% confidence interval of the mean. One-sample t-Test was performed with the alternative hypothesis being that energy dissipation of the designated heterogeneous variation is greater than that of its effective homogeneous counterpart. The high p-values in (a) and (b) show that at the 0.05 level elastic heterogeneity does not significantly enhance energy dissipation, while the low p-values in (c) and (d) indicate that at the 0.05 level inelastic heterogeneity leads to statistically significant promotion in energy dissipation.

greater than 0.95. If we now test the reverse hypothesis that heterogeneity leads to reduction in energy dissipation, all these five cases indeed show statistically significant reduction ($p<0.05$ with respect to the temporarily reversed *alternative hypothesis*) in energy dissipation ($\sim$5–10% decrease). In the 2D indentation model, the average differences in energy dissipation resulted from elastic heterogeneity are found to be limited within a narrow range of $\times 2\%$, as shown in Fig. 4(b). No statistically significant increase in energy dissipation is identified since $p \geq 0.3$ for all cases in Fig. 4(b). Results in Fig. 4(a) and (b) suggest that elastic heterogeneity of bone alone could not facilitate statistically significant increase in energy dissipation during the deformation modes we studied.

In contrast, Fig. 4(c) shows that for the 4-point bend model inelastic heterogeneity can increase energy dissipation up to 48%. Here, all cases show p-values less than 5×10^{-5}, suggesting that increases in energy dissipation due to inelastic heterogeneity are statistically significant. Similarly, Fig. 4(d) indicates that inelastic heterogeneity can cause a statistically significant ($p<0.005$) increase in energy dissipation for 2D indentation model. The average increase in energy dissipation reaches up to 15–30%. Moreover, Fig. 4(c) and (d) also show that energy dissipation due to inelastic heterogeneity increases with increase in σ_y/H. Within the reasonable range of $0.3<\sigma_y/H<0.6$, at least a 15% enhancement can be achieved for both 4-point bend and 2D indentation models. Therefore, Fig. 4 suggests that inelastic heterogeneity, rather than elastic heterogeneity, plays the dominant role in promoting energy dissipation in bone at least under the deformation modes examined here. This interesting result may arise from the fact that the inelastic deformation of any particular point in material is coupled with its local surrounding environment, which is quite different from a homogeneous material to a heterogeneous material. In a homogeneous material under indentation, for example, deformation is highly localized under the indenter and, hence, regions at the interior of the deformation zone will exhibit confinement effects. Further spreading of inelastic deformation would be mitigated. In a heterogeneous material, however, the deformation is more diffuse, thereby giving rise to more energy dissipation.

4. The effect of inelastic property heterogeneity on energy dissipation

Having shown that nanoscale inelastic heterogeneity promotes energy dissipation in bone, it is more important to advance further to identify parameters that facilitate maximum energy dissipation. Setting the experimentally extracted maps of inelastic properties as the base microstructural design, variations of inelastic heterogeneity near the base design are created to evaluate the impact of tuned heterogeneity on energy dissipation. Here we mainly focus on the variations of two important parameters that determine the COV of inelasticity, namely the standard deviation and the mean value of heterogeneous σ_y. Taking the heterogeneous σ_y maps obtained from experimental hardness H maps through assumed correlation σ_y=0.3H as the base designs, variations of standard deviation and mean value of σ_y can be achieved by

$$\sigma_{yi}^{new}=\overline{\sigma}_y^{ori}+\alpha(\sigma_{yi}^{ori}-\overline{\sigma}_y^{ori}) \tag{2}$$

and

$$\sigma_{yi}^{new}=\sigma_{yi}^{ori}+\beta\overline{\sigma}_y^{ori} \tag{3}$$

respectively. Here σ_{yi}^{ori} is the i-th individual yield stress in the original base map with mean value $\overline{\sigma}_y^{ori}$, σ_{yi}^{new} stands for the i-th yield stress after modification, and α and β are two constants controlling the extent of the introduced variations. Apparently, the variation defined by Eq. (2) alters the standard deviation by a factor of α, while keeping the mean value unchanged. On the contrary, the variation given by Eq. (3) adjusts the mean value by a magnitude of $\beta\overline{\sigma}_y^{ori}$, while keeping the standard deviation unchanged. Simulations based on these two types of variations allow us to evaluate the influences of the standard deviation and the mean value of the yield stress on energy dissipation separately. Ignoring the relatively small contributions of elastic heterogeneity on energy dissipation as demonstrated above, elasticity is assumed homogeneous and unchanged by taking the modulus as the mean value of the related experimental modulus map. As in Section 3, 16 heterogeneous cases including 4 original designs and 12 rotated derivatives are examined here.

Fig. 5(a) and (b) plots the variations of energy dissipation as a function of the standard deviation of σ_y with the mean value of σ_y unchanged. Each of the 16 cases studied is individually plotted in two figures. Curves with the same color correspond to four orientations (0°, 90°, 180°, and 270° rotations) of the same map. In general, inelastic energy dissipation increases with increase in standard deviation of σ_y no matter which simulation models were adopted. It should be pointed out that there is actually a limit on how much one can increase Std.(σ_y) following Eq. (2), since an overmuch increase in Std.(σ_y) will bring the lowest yield strength within the σ_y map down to zero or a negative value.

Fig. 5(c) and (d) depicts the energy dissipation variations as a function of the mean value of σ_y with Std.(σ_y) unchanged. Again, each of the 16 cases studied is plotted individually in these figures. In Fig. 5(c), each curve shows a peak within the investigated parameter space, indicating that there is a possible optimum $\overline{\sigma}_y/E$ ratio for facilitating energy dissipation. The estimated optimum $\overline{\sigma}_y/E$ from these 16 modeling cases is 0.037 ± 0.006, while the $\overline{\sigma}_y/E$ ratio from the experimental base microstructures is 0.027 ± 0.009 (taking σ_y/H as 0.3). Considering that the reasonable range of σ_y/H is actually $0.3<\sigma_y/H<0.6$, bone might have selected the optimal ratio of $\overline{\sigma}_y/E$ to achieve the maximum energy dissipation. However, under a compressive loading condition simulated by the 2D-indentation model, the results are quite different. As shown in Fig. 5(d), on average the extent of energy dissipation increases with decrease in $\overline{\sigma}_y/E$, although not every individual case follows the same trend. Likewise, there is also an apparent limit on how much one can decrease $\overline{\sigma}_y/E$ following Eq. (3),

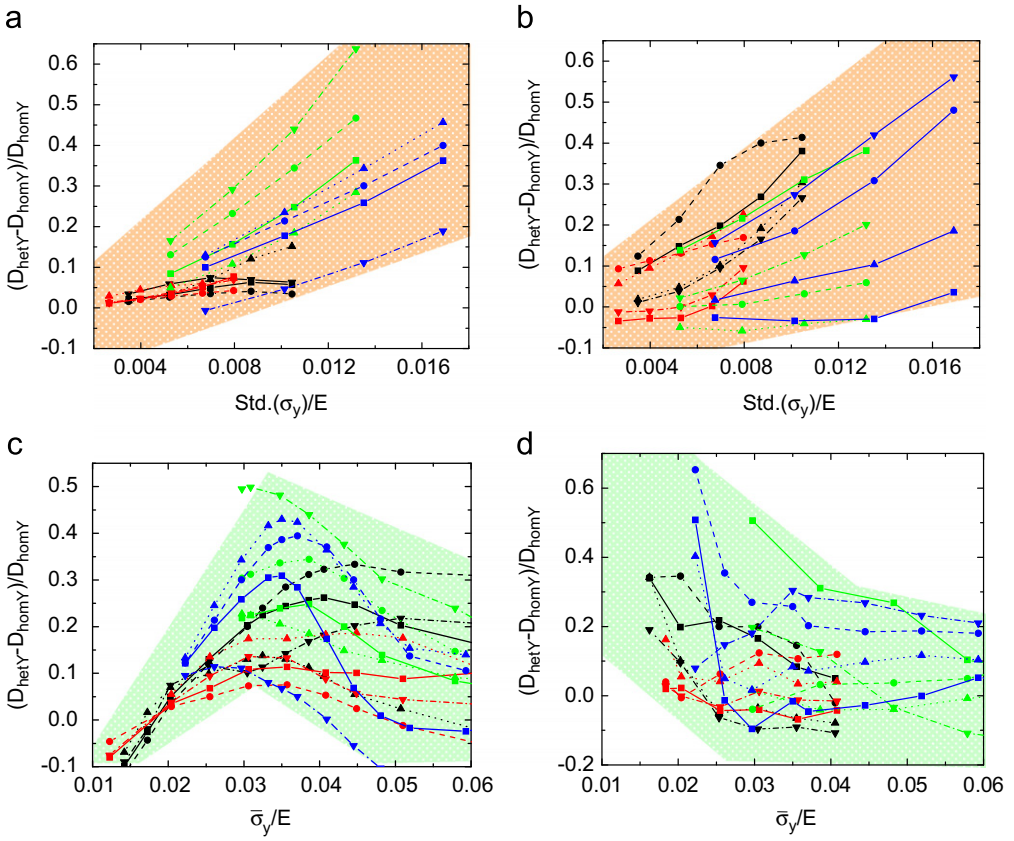

Fig. 5. Variation of enhancement in energy dissipation versus standard deviation ((a) and (b)) and mean value ((c) and (d)) of the inelastic yield stress normalized with E. (a) and (c) are the results from 4-point bend model, and (b) and (d) are the results from 2D indent model.

since an overmuch decrease in $\overline{\sigma}_y$ will force the lowest yield strength within the σ_y map down to zero or a negative value. The difference between Fig. 5(c) and (d) implies that the enhancement of energy dissipation with respect to the mean yield strength depends heavily on the stress state or loading mode experienced by the material. Therefore, heterogeneity in bone might be designed to have a $\overline{\sigma}_y/E$ ratio that maximizes energy dissipation under a local stress state resembling that ahead of a Mode-I crack under tension. Under a compressive loading condition, a general increase in trend in energy dissipation is observed with decrease in $\overline{\sigma}_y/E$.

5. Discussion and summary

In this paper, we quantified the size-dependence of heterogeneity of bovine cortical bone. To better understand the size-dependence of COV shown in Fig. 2(e), an idealized square model is constructed, as shown in Fig. 6(a): a two-phase composite model material with basic building block sizes of a_R and a_S for the hard/stiff and soft/compliant phases, respectively. These basic blocks construct the hard phase and soft phase clusters with sizes L_R and L_S, respectively. As shown in Fig. 6(b), the effective sampling size (e.g. the maximum indenter contact diameter) is marked with l. For an idealized case with square-shaped constituents (L_R=L_S=L) alternately populated within the region of interest, COV can be calculated as a function of the effective sampling size l using the methodology introduced earlier in Section 2. Assuming E_R/E_S=10 and taking any suitable choices of $a_R \le L$ and $a_S \le L$, Fig. 6(b) shows the calculated variation of COV versus the sampling size l for L=150, 500, and 1000 nm. It can be seen from Fig. 6(b) that the alternating square structure with L=150 nm shows a sharp COV transition at the probing size 200–250 nm. Such sharp transitions happen at much larger scales for the cases with L=500 nm and 1000 nm. This suggests that for length scale larger than the sizes of the most basic structural building blocks, the size-dependence of the heterogeneity in the composite can be altered by changing the size of phase clusters. That is, given the sizes of the basic building blocks one can achieve the same heterogeneity at different length scales simply by adjusting the size of phase clusters. For example, Fig. 6(b) shows that we can achieve COV=0.4 at scales 150, 400, and 800 nm taking the cluster sizes L=150, 500, and 1000 nm, respectively. The two-phase composite model is an idealized approximation meant to explore trends in size-dependent heterogeneity and homogenization. While bone can be considered to be a two-phase composite with rigid (mineral) and compliant (organic) phases with a complicated hierarchical microstructure, the geometry and spatial arrangement of the phases departs from that assumed

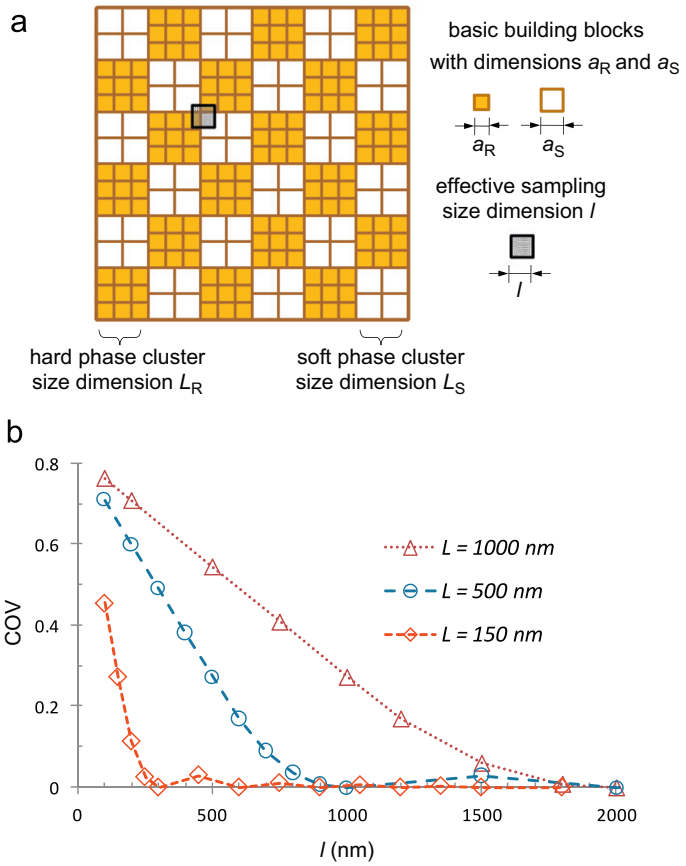

Fig. 6. (a) Schematic of a two-phase composite material with basic building block sizes of a_R and a_S for the hard and soft phases, respectively. These basic blocks can form hard and soft phase clusters with sizes L_R and L_S, respectively. The effective sampling size dimension of a probe (e.g. an indenter tip) is denoted by l. (b) Calculated variation of COV as a function of probing size l for an idealized case with square shaped constituents (L_R=L_S=L) is alternatively populated. Here modulus ratio of the two phases is assumed as E_R/E_S=10 and L is taken as 150, 500, and 1000 nm, respectively.

in the model, and hence, a direct quantitative comparison with experimental data is precluded. However, the model does provide significant scientific information on qualitative trends of the effect of phase volume fraction, cluster size, and cluster aspect ratio on heterogeneity via parametric assessment. Within the 50–500 nm length scale, the bone tissue can be considered consisting of a more rigid fibrillar space and a relatively compliant extra-fibrillar space (Hellmich and Ulm, 2003). For wet tissue densities ranging from 1.7 to 2.3 g/cm^3, the estimated extra-fibrillar volume fraction ranges from 0.3 to 0.7 (Hellmich and Ulm, 2003). If we take the typical mammalian cortical bone density to be ~1.8–2 g/cm^3 (Lai et al., 2005; Tai, 2007), the extra-fibrillar volume fraction would be given as ~0.5–0.6. In addition to the 0.5 volume fraction and square shape shown in Fig. 6(a), we have performed a parametric study using this idealized composite model with different volume fractions (1/3 to 2/3) and cluster aspect ratios (up to 1:5) and found a similar general trend, i.e. there is a sharp COV transition at probing size ~200–300 nm.

For bone, taking the collagen fibril's diameter (~150 nm in the bone samples tested in the present study) and its axial repeat length (~67 nm) as the reference for the basic building block size, this simple model suggests that nature has the freedom to build a microstructure with various characteristic heterogeneity sizes larger than 200 nm. However, in order to achieve both high strength and optimum flaw tolerance, as pointed out earlier in the introduction, there should be an upper limit (~30–200 nm) on the phase cluster feature size (Gao et al., 2003). Considering the hierarchical structural feature of bone (Fratzl and Weinkamer, 2007), other characteristic sizes are expected to exist at different length scales. Indeed, in a recent study (Gupta et al., 2006) a larger characteristic length scale due to the periodicity of the osteonal lamellae was identified at a higher level. With the length scale covered in this paper, we would not be able to capture higher length scale mechanisms. There are many possible energy dissipation mechanisms that exist in bone at various length scales (Tai et al., 2005; Bonderer et al., 2008), e.g. debonding of mineral–organic interfaces, collagen fibril shear, crosslink scission, denaturation and failure of collagen fibrils, crack formation and propagation, mineral displacement, deformation and structural phase transformation, viscous stretching of the organic component, and rupture of self-healing sacrificial bonds. In this paper, the additional mechanism of nanoscale heterogeneity is explored, which is expected to act in parallel with and be coupled to other mechanisms. For example, yielding within each localized spatial region ultimately

will be controlled by one of the above listed molecular-level mechanisms. Spatial heterogeneity can, for example, result in confinement and constraint which may enhance how molecular-based plasticity progresses.

In summary, the results obtained in the present study suggest that a nanoscale characteristic size exists in bone. Size-dependent heterogeneity is much more pronounced below this critical size and stays relatively low beyond this size. This characteristic size is estimated to be around 200 nm, which is on the order of 1–2 times the diameter of individual collagen fibrils. Detailed computational simulations incorporating experimentally measured nanoscale heterogeneities show that the heterogeneity of inelasticity, rather than elasticity, plays the dominant role in promoting energy dissipation in bone. The substantial mechanisms for this phenomenon require further investigations. Nevertheless, one important contributing factor emerging from this work is that the natural heterogeneity found in bone can extend plastic deformation over larger distances from a notch tip or indenter tip, thereby resulting in considerably larger inelastic zones in comparison to its corresponding homogenous case (Tai et al., 2007). A parametric study suggests an optimum $\overline{\sigma}_y/E$ ratio for improving energy dissipation under a local stress state resembling that ahead of a Mode-I crack-like notch. Our findings suggest that the size-dependent inelastic heterogeneity identified in bone is advantageous for its mechanical performance since it promotes energy dissipation at nanoscale and simultaneously reduces the heterogeneity-induced stress concentration and strain localization at higher length scales. These results also provide useful guidelines for designing bio-inspired, spatially heterogeneous nanocomposites with superior mechanical performance. The enhanced energy dissipation due to nanoscale heterogeneity may serve as one additional toughening mechanism among many possible mechanisms functioning at different length scales for bone.

Acknowledgements

The authors would like to acknowledge the MIT Department of Materials Science and Engineering Nanomechanical Testing Facility for the experiments conducted here. Thanks are due to A. Schwartzman for his help with the experiments. We also gratefully acknowledge support from the National Science Foundation MIT Center for Materials Science and Engineering (MRSEC), the US Army through the MIT Institute for Soldier Nanotechnologies (contract number DAAD-19–02-D0002), the Advanced Materials for Micro and Nano Systems Programme and the Computational Systems Biology Programme of the Singapore-MIT Alliance (SMA), the Singapore-MIT Alliance for Research and Technology (SMART), Raytheon, Inc., and the National Security Science and Engineering Faculty Fellowship (NSSEFF) Program. HY gratefully acknowledges the support from the Program for New Century Excellent Talents in University from the Ministry of Education of China.

References

Bonderer, L.J., Studart, A.R., Gauckler, L.J., 2008. Bioinspired design and assembly of platelet reinforced polymer films. Science 319 (5866), 1069–1073.
Brockenbrough, J.R., Wienecke, H.A., Suresh, S., 1991. Deformation of metal–matrix composites with continuous fibers—geometrical effects of fiber distribution and shape. Acta metallurgica et Materialia 39, 735–752.
Ciarelli, T.E., Fyhrie, D.P., Schaffler, M.B., Goldstein, S.A., 2000. Variations in three-dimensional cancellous bone architecture of the proximal femur in female hip fractures and in controls. Journal of Bone and Mineral Research 15, 32–40.
Currey, J., 2005. Structural heterogeneity in bone: good or bad? Journal of Mussuloskeletal and Neuronal Interactions 5 (4), 317
Dao, M., Chollacoop, N., Van Vliet, K.J., Venkatesh, T.A., Suresh, S., 2001. Computational modeling of the forward and reverse problems in instrumented sharp indentation. Acta Materialia 49 (19), 3899–3918.
Feng, G., Qu, S., Huang, Y., Nix, W.D., 2007. An analytical expression for the stress field around an elastoplastic indentation/contact. Acta Materialia 55 (9), 2929–2938.
Fratzl, P., Weinkamer, R., 2007. Nature's hierarchical materials. Progress in Materials Science 52 (8), 1263–1334.
Gao, H., Ji, B., Jager, I.L., Arzt, E., Fratzl, P., 2003. Materials become insensitive to flaws at nanoscale: lessons from nature. Proceedings of the National Academy of Sciences U.S.A 100 (10), 5597–5600.
Gouldstone, A., Chollacoop, N., Dao, M., Li, J., Minor, A.M., Shen, Y.L., 2007. Indentation across size scales and disciplines: recent developments in experimentation and modeling. Acta Materialia 55 (12), 4015–4039.
Gupta, H.S., Stachewicz, U., Wagermaier, W., Roschger, P., Wagner, H.D., Fratzl, P., 2006. Mechanical modulation at the lamellar level in osteonal bone. Journal of Material Research 21 (8), 1913–1921.
Hellmich, C., Ulm, F.J., 2003. Average hydroxyapatite concentration is uniform in the extracollagenous ultrastructure of mineralized tissues: evidence at the 1–10 micron scale. Biomechanics and Modelling in Mechanobiology 2 (1), 21–36.
Kasiri, S., Taylor, D., 2008. A critical distance study of stress concentrations in bone. Journal of Biomechanics 41 (3), 603–609.
Lai, Y.M., Qin, L., Hung, V.W.Y., Chan, K.M., 2005. Regional differences in cortical bone mineral density in the weight-bearing long bone shaft—a pQCT study. Bone 36 (3), 465–471.
Lakes, R., 1993. Materials with structural hierarchy. Nature 361 (6412), 511–515.
Morgan, E.F., Bayraktar, H.H., Keaveny, T.M., 2003. Trabecular bone modulus-density relationships depend on anatomic site. Journal of Biomechanics 36 (7), 897–904.
Munch, E., Launey, M.E., Alsem, D.H., Saiz, E., Tomsia, A.P., Ritchie, R.O., 2008. Tough, bio-inspired hybrid materials. Science 322 (5907), 1516.
Oliver, W.C., Pharr, G.M., 1992. An improved technique for determining hardness and elastic modulus using load and displacement sensing indentation experiments. Journal of Material Research 7, 1564–1583.
Peterlik, H., Roschger, P., Klaushofer, K., Fratzl, P., 2005. From brittle to ductile fracture of bone. Nature Materials 5 (1), 52–55.
Pharr, G.M., Bolshakov, A., 2002. Understanding nanoindentation unloading curves. Journal of Material Research 17 (10), 2660–2671.
Phelps, J.B., Hubbard, G.B., Wang, X., Agrawal, C.M., 2000. Microstructural heterogeneity and the fracture toughness of bone. Journal of Biomedical Materials Research 51 (4), 735–741.
Pope, M.H., Outwater, J.O., 1974. Mechanical properties of bone as a function of position and orientation. Journal of Biomechanics 7, 61–66.
Rho, J.Y., Zioupos, P., Currey, J.D., Pharr, G.M., 2002. Microstructural elasticity and regional heterogeneity in human femoral bone of various ages examined by nano-indentation. Journal of Biomechanics 35, 189–198.

Shen, Y.L., Finot, M., Needleman, A., Suresh, S., 1994. Effective elastic modulus of two-phase composites. Acta Metallurgica et Materiala 42 (1), 77–97.
Shen, Y.L., Finot, M., Needleman, A., Suresh, S., 1995. Effective plastic response of two-phase composites. Acta Metallurgica et Materialia 43 (4), 1701–1722.
Suresh, S., 2001. Graded materials for resistance to contact deformation and damage. Science 292 (5526), 2447–2451.
Tai, K., 2007. Nanomechanics and ultrastructural studies of cortical bone: fundamental insights regarding structure–function, mineral–organic force mechanics interactions, and heterogeneity. Ph.D. Thesis, Department of Materials Science and Engineering, MIT.
Tai, K., Dao, M., Suresh, S., Palazoglu, A., Ortiz, C., 2007. Nanoscale heterogeneity promotes energy dissipation in bone. Nature Materials 6 (6), 454–462.
Tai, K., Qi, H.J., Ortiz, C., 2005. Effect of mineral content on the nanoindentation properties and nanoscale deformation mechanisms of bovine tibial cortical bone. Journal of Materials Science.—Materials in Medicine 16, 947–959.
Wagermaier, W., Gupta, H.S., Gourrier, A., Paris, O., Roschger, P., Burghammer, M., Riekel, C., Fratzl, P., 2007. Scanning texture analysis of lamellar bone using microbeam synchrotron X-ray radiation. Journal of Applied Crystallography 40, 115–120.
Yeni, Y.N., Hou, F.J., Vashishth, D., Fyhrie, D.P., 2001. Trabecular shear stress in human vertebral cancellous bone: intra-and inter-individual variations. Journal of Biomechanics 34 (10), 1341–1346.